

Exploring Altermagnetism in Orthorhombic $Pnma$ structure through Group Theory and DFT Calculations

Suman Rooj^{†,*}, Sugandha Saxena,[†] and Nirmal Ganguli[‡]

Department of Physics, Indian Institute of Science Education and Research Bhopal, Bhauri, Bhopal 462066, India

(Dated: 11 June 2024)

Antiferromagnetism, initially considered interesting but useless, recently emerged as one of the most promising magnetic phases for technology. Recently, a low symmetry antiferromagnetic phase, known as altermagnetic phase, have been discovered, where no time reversal (\mathcal{T}) symmetry is observed in spite of a vanishing net magnetization, leading to non-degenerate bands from the opposite magnetic sublattices. In this work, we consider two representatives of orthorhombic $Pnma$ space group, namely, BiFeO_3 and CaMnO_3 and find altermagnetic lowest energy phase in both from our density functional theory calculations. We find a substantial spin-splitting in both systems along a high-symmetry path in the Brillouin zone without considering the spin-orbit interaction (SOI). Detailed features of the band dispersion obtained from our calculation confirm the lifting of sublattice spin degeneracy only in the k_y - k_z plane while preserving the spin degeneracy in the other planes of the Brillouin zone. We provide a comprehensive symmetry analysis based on the magnetic space group (MSG) to explain our DFT findings and an insightful symmetry-allowed model Hamiltonian, which qualitatively agrees with our results. Additionally, we extend our symmetry analysis to encompass two other potential MSGs within the $Pnma$ space group that may host the spin-splitting phenomenon without considering SOI and the likely form of their Hamiltonian. These detailed studies pave the way for a deeper understanding of the spin-splitting phenomena within the $Pnma$ space group, offering insights into the intricate interplay between symmetry and electronic as well as magnetic properties.

I. INTRODUCTION

Magnetism in quantum materials and heterostructures exhibits fascinating scientific phenomena besides presenting exciting possibilities for new technology. The interplay between three fundamental ingredients, magnetism, spin-orbit interaction, and crystal symmetry, may lead to many exotic features in a quantum material, including topologically nontrivial properties, Rashba-Dresselhaus interaction, spin-Hall effect [1, 2]. Among these, antiferromagnetic spintronics emerges as a promising frontier, wherein materials with significant spin-orbit interaction enable THz-speed computational processing and nonvolatile memory storage through spin-texture manipulation via spin-orbit torque [3]. However, this paradigm undergoes a significant shift following the theoretical prediction and experimental verification of an interesting collinear antiferromagnetic phase, known as altermagnets, where the bands from the opposite magnetic sublattices are non-degenerate [4–9]. Altermagnetic materials present fascinating attributes where time-reversal symmetry-breaking responses and spin-polarization emerge independent of spin-orbit interaction, accompanied by the collinear antiparallel magnetic order, leading to a vanishing net magnetization [6, 7]. RuO_2 , a workhorse material of altermagnetism, showcases spin-polarization, resulting in a spin-splitter torque, which holds promise for manipulating spin-

textures [10, 11]. Besides the spin-splitter torque, some of the altermagnetic materials have been theoretically predicted and experimentally validated to host various other interesting phenomena. For instance, the anomalous Hall effect (AHE) has been experimentally demonstrated in some altermagnets such as MnTe , Mn_5Si_3 , and RuO_2 [12–15]. Additionally, giant tunneling magnetoresistance has been theoretically predicted in the $\text{RuO}_2|\text{TiO}_2|\text{RuO}_2$ heterostructure [16]. Furthermore, theoretical predictions of chiral magnons, crystal Nernst, and crystal thermal Hall effect have been reported in RuO_2 [17, 18]. Experimental observations have been made on the giant spin polarization in the non-relativistic limit in MnTe [19]. These collective insights illustrate the emerging landscape of altermagnetism, perpetuating the ongoing pursuit of suitable altermagnetic materials.

In this work, based on the crystal symmetry, we identify two centrosymmetric materials: bulk orthorhombic BiFeO_3 (BFO) and CaMnO_3 (CMO), both belonging to nonsymmorphic $Pnma$ space group, as potential altermagnets. Employing first-principles density functional theory (DFT) calculations, we investigate the electronic structure of BFO and CMO in their orthorhombic structure. After finding the ground state magnetic arrangement for both systems, we critically examine the spin-splitting behavior with and without spin-orbit interaction within DFT calculations. In this study, we primarily focus on spin-splitting behavior without spin-orbit interaction. Additionally, we explain our findings using magnetic space group (MSG) symmetry analysis and an insightful analytical model. Our prediction of the spin-splitting effects without spin-orbit interaction conclusively designates these two compounds as altermag-

* Email: suman18@iiserb.ac.in

† These two authors contributed equally

‡ Email: NGanguli@iiserb.ac.in

TABLE I. The lattice constants of BiFeO₃ and CaMnO₃, as obtained from experiments are tabulated here [20, 21].

Crystal structure	a (Å)	b (Å)	c (Å)
BiFeO ₃	5.61	7.97	5.65
CaMnO ₃	5.33	7.50	5.31

nets. We further anticipate the possible spin-splitting behavior for two other potential MSGs within the $Pnma$ space group and the probable form of model Hamiltonians. The remainder of the article is structured as follows: The crystal structure and calculation methodologies are described in Sec. II. In Sec. III, we rigorously discuss the results encompassing the electronic structure and symmetry analysis of our investigation. Finally, we summarize our work in Sec. IV.

II. CRYSTAL STRUCTURE AND METHODOLOGY

Bulk BiFeO₃ (BFO) and CaMnO₃ (CMO) crystallize in a centrosymmetric orthorhombic structure with $Pnma$ space group. The Perovskite oxides BFO and CMO may be described by a general formula ABO₃, with A = Bi/Ca, B = Fe/Mn. The A, B, and O sites occupy the Wyckoff positions $4c$, $4b$, and $(8d, 4c)$, respectively [23, 24]. Fig. 1(a) depicts a unit cell of ABO₃, illustrating corner sharing BO₆ octahedra, while A atoms occupy the interstitial sites. The experimental lattice parameters for both compounds are tabulated in Table I. The total energy, electronic structure, magnetic properties, and spin-orbit interaction calculations are carried out within density functional theory (DFT) as implemented in the VASP code [25, 26]. The projector augmented wave (PAW) method is employed for the potential description alongside a plane wave basis set with a 500 eV energy cutoff for expanding the wavefunctions [27]. The exchange-correlation functional is treated within the generalized gradient approximation (GGA) [28] with Hubbard- U [29] correction of $U_{\text{eff}} = U - J = 4$ and 3 eV for Fe- $3d$ and Mn- $3d$ states respectively to take care of the strong Coulomb correlation in BFO and CMO [30, 31]. The integration over the Brillouin zone is performed using a $5 \times 3 \times 5$ Γ -centered k -point mesh for the unit cell within the corrected tetrahedron method [32]. The electronic convergence threshold of 10^{-6} eV is employed for all calculations. Atomic positions and lattice vectors are optimized by minimizing the Hellman-Feynman force on each atom up to a threshold value of 10^{-2} eV/Å.

TABLE II. Different magnetic configurations and their relative energies in the meV unit are listed here for the unit cell of both systems, BFO and CMO.

Magnetic Configuration	BFO	CMO
FM	825.97	184.49
A - AFM	515.04	72.92
C - AFM	233.63	31.34
G - AFM	0	0

III. RESULT AND DISCUSSION

A. Electronic structure and magnetic properties

The compounds BiFeO₃ (BFO) and CaMnO₃ (CMO) are found in nominal oxidation states Bi³⁺Fe³⁺O₃²⁻ and Ca²⁺Mn⁴⁺O₃²⁻, respectively, in their bulk forms. We start by comparing the total energies of different possible antiferromagnetic configurations, namely, A-type, C-type, and G-type antiferromagnets (AFMs) as depicted in the Fig. 1(d),(e), and (f), which results in no net magnetic moment, alongside the ferromagnetic configuration. Table II shows the relative energies for different magnetic configurations, suggesting G-type AFM to have the lowest energy for both BFO and CMO. In G-type AFM, the magnetic moments are antiparallel for the nearest neighbors in all directions, as shown in Fig. 1(f). Unless stated otherwise, the subsequent results regarding the unit cell correspond to the lowest energy G-type AFM configuration. However, CMO exhibits complex magnetic behavior at low temperatures, showing a paramagnet to AFM transition below the Néel temperature $T_N \sim 125$ K, and a weak ferromagnetic behavior below ~ 10 K in its ground state [33]. On the other hand BFO shows antiferromagnetic ordering below the Néel temperature ~ 640 K [34].

The band dispersion for both spin sublattices, marked as spin A and spin B for BFO and CMO, shown in Fig. 2(a) and Fig. 3(a), suggests an indirect band gap of ~ 1.91 eV for BFO and ~ 1.23 eV for CMO. We find projected magnetic moments of $\sim 4.16 \mu_B$ and $\sim 2.74 \mu_B$ at the Fe and Mn sites in BFO and CMO, respectively, suggesting a high spin configuration. We note that projected magnetic moments are usually underestimated within a plane wave basis set. The calculated band gap of CMO and the magnetic moment of the Mn atom are in good agreement with the experimentally reported range of ~ 1.1 - 1.2 eV [35] and $\sim 3 \mu_B$ [36], respectively. On the other hand, due to limited experimental studies on orthorhombic BFO, the experimental band gap the magnetic moment of the Fe atom remains inaccessible. The band dispersions, shown in Fig. 2(a) and Fig. 3(a) for BFO and CMO, respectively, reveals a perfect overlap of both spins for both systems along the chosen high-symmetry directions. However, from a symmetry perspective, these compounds break the combined inversion | time reversal (\mathcal{PT}) and combined spin rotation | translation ($U\tau$) symmetries [9], as illustrated in Fig. 1(c).

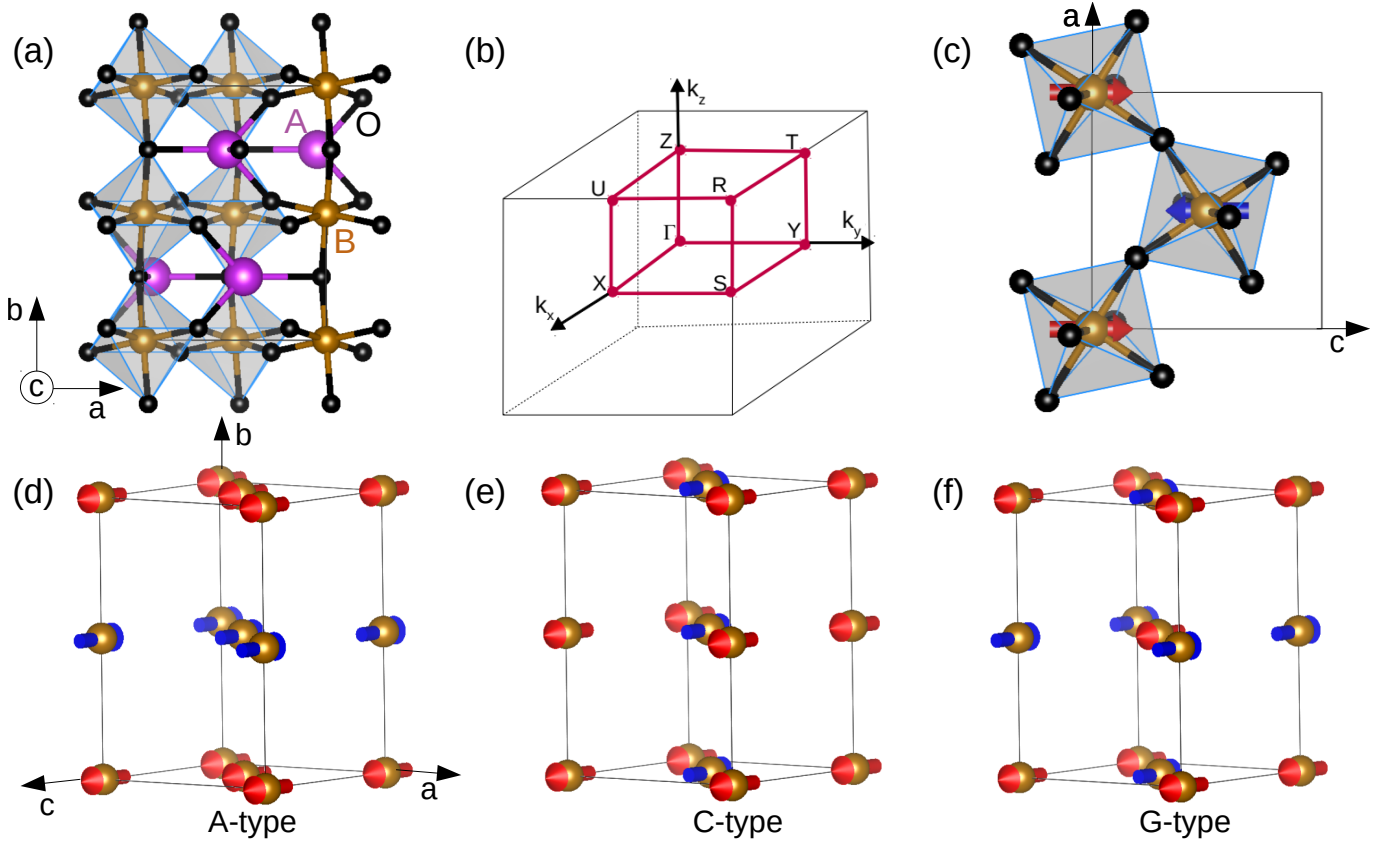


FIG. 1. Panel (a) and (b) display an orthorhombic unit cell of ABO₃ Perovskite oxide structure, highlighting the corner-sharing BO₆ octahedra and the Brillouin zone, respectively, while (c) depicts a view on the *ac* plane, illustrating the broken $U\tau(\frac{1}{2}\frac{1}{2})$ symmetry. The A, C, and G-type antiferromagnetic configurations are illustrated in (d), (e), and (f), respectively. Crystal structure and magnetic configuration illustrations were prepared using VESTA software [22].

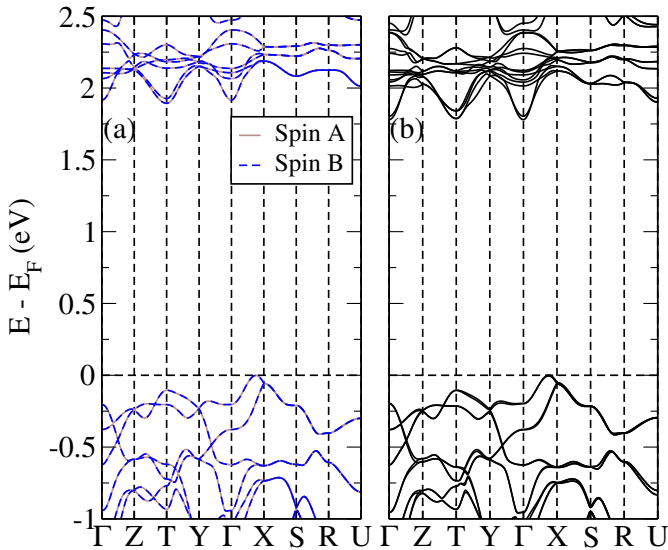


FIG. 2. Spin-polarized band dispersion for BFO from both spins marked as spin A and spin B is depicted in (a), while (b) represents the band structure considering spin-orbit interaction.

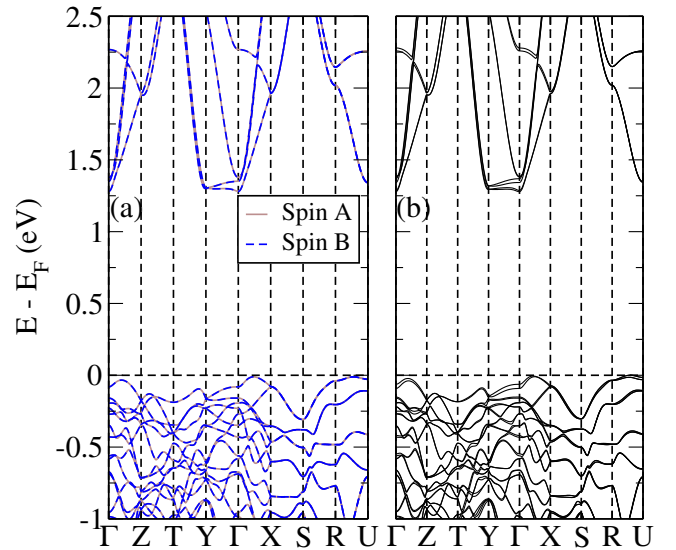


FIG. 3. Spin-polarized band dispersion for CMO from both spins marked as spin A and spin B is depicted in (a), while (b) represents the band dispersion considering spin-orbit interaction.

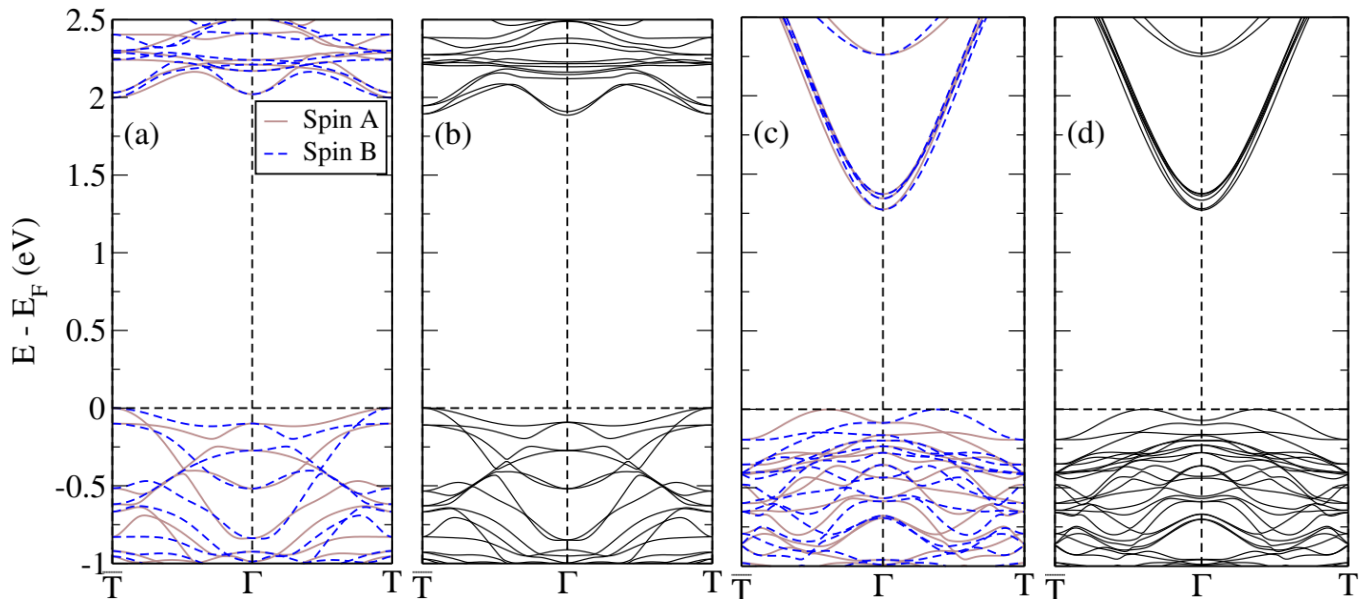


FIG. 4. Spin-polarized band dispersion for BFO and CMO for both spins marked as Spin A and Spin B are displayed in (a) and (c), while panel (b) and (d) shows the band dispersion with considering spin-orbit interaction along $\bar{T} \rightarrow \Gamma \rightarrow T$ direction.

TABLE III. The relative energies for the unit cell along different crystallographic directions including spin-orbit interaction in meV per formula unit are tabulated here.

Spin quantization axis	BFO	CMO
(100)	0.265	0.055
(010)	0.497	0.017
(001)	0.0	0.0
(110)	0.355	0.027

As a consequence, the opposite spin bands cannot be degenerate everywhere in the Brillouin zone, as confirmed along the high-symmetry $\bar{T} \rightarrow \Gamma \rightarrow T$ direction for both compounds, displayed in Fig. 4(a) and Fig. 4(c) for BFO and CMO, respectively.

Upon considering the spin-orbit interaction (SOI) in our DFT calculations, we find an anisotropy in the spin-quantization axis based on the different crystallographic directions. Here, we calculate the relative energies for different spin quantization directions *viz.* (100), (010), (001), and (110) for both BFO and CMO, and tabulate the results in Table III. The table reveals (001) as the preferred spin-quantization direction for both compounds. The band dispersion changes only slightly upon considering SOI, as evident from Fig. 2(b) and Fig. 3(b).

B. Symmetry analysis

1. Space Group Symmetry

In this section, we discuss in detail the space group symmetries and magnetic space group (MSG) symme-

tries without spin-orbit interaction (SOI) for both compounds. BFO and CMO have the same orthorhombic symmetry as discussed in Sec. II; hence, all the symmetry analyses and conclusions drawn are equally applicable to both compounds. The $Pnma$ space group contains 8 unitary symmetry operations ($G \equiv G_U$) listed in Table IV. Here, 1 and -1 are the identity and the spatial inversion operation; $2_{100}, 2_{010}, 2_{001}$ are the two-fold (π) anticlockwise rotation about the [100], [010], [001] axes, respectively; $m_{100}, m_{010}, m_{001}$ are the reflections in [100], [010], [001] planes, respectively; vectors $(\frac{1}{2} \frac{1}{2} \frac{1}{2})$, $(0 \frac{1}{2} 0)$, and $(\frac{1}{2} 0 \frac{1}{2})$ are the nonprimitive translations. In this paper, we adopt all the notations similar to the Bilbao Crystallographic Server [23, 37].

Considering the magnetic arrangement of a system, the combined structural and magnetic symmetry may be described by a magnetic space group (MSG), where the time reversal operator \mathcal{T} may combine with some of the group elements [38]. For our purposes, the MSG of G-type antiferromagnetic BFO and CMO is $Pnm'a'$ without considering spin-orbit interaction [39, 40]. The operations of MSG $Pnm'a'$ are explicitly listed in Table V, which include half of the elements of G ($Pnma$) as unitary operations (G_U), while the rest are antiunitary $G_{AU} = \mathcal{T}(G - G_U)$.

2. Spin-splitting without SOI

Here, we discuss the splitting of the opposite-spin bands in different parts of the Brillouin zone (BZ) without considering SOI in our calculations. Although the band dispersions without SOI depicted in Fig. 2(a)

TABLE IV. Different symmetry operations (G) of the space group $Pnma$.

$\{1 0\}:(x, y, z) \rightarrow (x, y, z)$	$\{2_{010} 0 \frac{1}{2} 0\}:(x, y, z) \rightarrow (-x, y + \frac{1}{2}, -z)$
$\{2_{001} \frac{1}{2} 0 \frac{1}{2}\}:(x, y, z) \rightarrow (-x + \frac{1}{2}, -y, z + \frac{1}{2})$	$\{2_{100} \frac{1}{2} \frac{1}{2} \frac{1}{2}\}:(x, y, z) \rightarrow (x + \frac{1}{2}, -y + \frac{1}{2}, -z + \frac{1}{2})$
$\{-1 0\}:(x, y, z) \rightarrow (-x, -y, -z)$	$\{m_{010} 0 \frac{1}{2} 0\}:(x, y, z) \rightarrow (x, -y + \frac{1}{2}, z)$
$\{m_{001} \frac{1}{2} 0 \frac{1}{2}\}:(x, y, z) \rightarrow (x + \frac{1}{2}, y, -z + \frac{1}{2})$	$\{m_{100} \frac{1}{2} \frac{1}{2} \frac{1}{2}\}:(x, y, z) \rightarrow (-x + \frac{1}{2}, y + \frac{1}{2}, z + \frac{1}{2})$

TABLE V. Different symmetry operations of the magnetic space group for G-type AFM without SOI: $Pnm'a'$.

G_U (Unitary)	G_{AU} (Antiunitary) = $\mathcal{T}(G - G_U)$
$\{1 0\}:(x, y, z) \rightarrow (x, y, z)$	$\mathcal{T}\{2_{001} \frac{1}{2} 0 \frac{1}{2}\}:(x, y, z) \rightarrow (-x + \frac{1}{2}, -y, z + \frac{1}{2})$
$\{2_{100} \frac{1}{2} \frac{1}{2} \frac{1}{2}\}:(x, y, z) \rightarrow (x + \frac{1}{2}, -y + \frac{1}{2}, -z + \frac{1}{2})$	$\mathcal{T}\{2_{010} 0 \frac{1}{2} 0\}:(x, y, z) \rightarrow (-x, y + \frac{1}{2}, -z)$
$\{-1 0\}:(x, y, z) \rightarrow (-x, -y, -z)$	$\mathcal{T}\{m_{001} \frac{1}{2} 0 \frac{1}{2}\}:(x, y, z) \rightarrow (x + \frac{1}{2}, y, -z + \frac{1}{2})$
$\{m_{100} \frac{1}{2} \frac{1}{2} \frac{1}{2}\}:(x, y, z) \rightarrow (-x + \frac{1}{2}, y + \frac{1}{2}, z + \frac{1}{2})$	$\mathcal{T}\{m_{010} 0 \frac{1}{2} 0\}:(x, y, z) \rightarrow (x, -y + \frac{1}{2}, z)$

and Fig. 3(a) for BFO and CMO, respectively, do not exhibit any spin-splitting feature, upon examining the band dispersion along the high-symmetry direction $\bar{\Gamma}(0, -\frac{\pi}{b}, \frac{\pi}{c}) \rightarrow \Gamma \rightarrow \bar{\Gamma}(0, \frac{\pi}{b}, \frac{\pi}{c})$, pronounced spin-splitting is observed from Fig. 4(a) and Fig. 4(c) for BFO and CMO, respectively. To further elucidate the spin-splitting, we have plotted the 3D band dispersion for a select pair of bands in different planes of the BZ. The spin degeneracy remains protected in the $k_z = 0$ plane, as seen from the isoenergetic contour for $E - E_F = -0.5$ eV in the k_x - k_y and the 3D band dispersion as a function of (k_x, k_y) , displayed in Fig. 5(b) and Fig. 5(c), respectively, for the pair of bands within a small energy range $[-0.6, -0.4]$ eV relative to the Fermi level, intersecting a horizontal red dashed line shown in Fig. 5(a). Further, $k_y = 0$ plane also preserves the spin degeneracy, as seen from isoenergetic contour for $E - E_F = -0.5$ eV displayed in Fig. 5(d) for the same pair of bands. However, isoenergetic contour for $E - E_F = -0.5$ eV in the k_y - k_z plane and the the 3D band dispersion as a function of (k_y, k_z) for $k_x = 0$, shown in Fig. 5(e) and Fig. 5(f), respectively, for the same pair of bands exhibit a pronounced spin-splitting. The nature of the isoenergetic contour in the k_y - k_z plane, as seen from Fig. 5(e) unequivocally confirms the altermagnetic feature in BFO. Likewise, the 3D band dispersion and isoenergetic contour plots in various planes, depicted in Fig. 6, also unveil altermagnetic features in CMO.

3. Magnetic space group symmetry and spin splitting

The group of wave vectors at the high-symmetry points in the BZ shown in Fig. 1 (b) preserve all the symmetry operations of the MSG $Pnm'a'$ that contain both unitary and antiunitary operations. The antiunitary operations flip the spin, keeping the coordinate of the high-symmetry points invariant and imposing the spin degeneracy, as evident from Fig. 2(a) and Fig. 3(a) for BFO and CMO, respectively. $(u, v, 0)$ with $(u, v) \in ([-\pi/a, \pi/a], [-\pi/b, \pi/b])$ represents a generic \vec{k} -vector in

the k_x - k_y plane. The symmetry operations in the MSG $Pnm'a'$ that leave a generic \vec{k} -vector in the k_x - k_y plane invariant are

$$\begin{aligned} &\{1|0\} : (u, v, 0) \rightarrow (u, v, 0) \text{ and} \\ &\mathcal{T}\left\{2_{001}\left|\frac{1}{2} 0 \frac{1}{2}\right.\right\} : (u, v, 0) \rightarrow (u, v, 0), \end{aligned} \quad (1)$$

as seen from Table V. The antiunitary operation $\mathcal{T}\{2_{001}|\frac{1}{2} 0 \frac{1}{2}\}$ that connects both magnetic sublattices ensures the spin degeneracy throughout the entire k_x - k_y plane for both compounds, as seen from Fig. 5(b),(c) and Fig. 6(b),(c).

Similarly, considering $(u, 0, w)$ as a generic coordinate of a \vec{k} in the k_x - k_z plane, we find the symmetry operations of the MSG $Pnm'a'$ that keep it invariant are (see Table V)

$$\begin{aligned} &\{1|0\} : (u, 0, w) \rightarrow (u, 0, w) \text{ and} \\ &\mathcal{T}\left\{2_{010}\left|0 \frac{1}{2} 0\right.\right\} : (u, 0, w) \rightarrow (u, 0, w). \end{aligned} \quad (2)$$

The antiunitary operation $\mathcal{T}\{2_{010}|0 \frac{1}{2} 0\} : (u, 0, w)$ connecting both spin sublattices preserves a spin degeneracy in this plane, as confirmed from the isoenergetic contours in Fig. 5(d) and Fig. 6(d).

When we consider the k_y - k_z plane, a generic \vec{k} -vector is represented with the coordinates $(0, v, w)$. The symmetry operations in the MSG $Pnm'a'$ that keep the \vec{k} -vector invariant are (see Table V)

$$\begin{aligned} &\{1|0\} : (0, v, w) \rightarrow (0, v, w) \text{ and} \\ &\left\{m_{100}\left|\frac{1}{2} \frac{1}{2} \frac{1}{2}\right.\right\} : (0, v, w) \rightarrow (0, v, w). \end{aligned} \quad (3)$$

None of these symmetry operations connect the magnetic sublattices with opposite spins, leading to broken spin degeneracy of the bands in this plane, as evident from Fig. 5(e),(f) and Fig. 6(e),(f), except for the two nodes at $k_y = 0$ and the other two nodes at $k_z = 0$ (see isoenergetic contour in Fig. 5(e) for BFO and Fig. 6(e) for

TABLE VI. Different symmetry operations of the magnetic space group for A-type AFM without SOI: $Pn'm'a$.

G_U (Unitary)	G_{AU} (Antiunitary) = $\mathcal{T}(G - G_U)$
$\{1 0\}:(x, y, z) \rightarrow (x, y, z)$	$\mathcal{T}\{2_{010} 0 \frac{1}{2} 0\}:(x, y, z) \rightarrow (-x, y + \frac{1}{2}, -z)$
$\{2_{001} \frac{1}{2} 0 \frac{1}{2}\}:(x, y, z) \rightarrow (-x + \frac{1}{2}, -y, z + \frac{1}{2})$	$\mathcal{T}\{2_{100} \frac{1}{2} \frac{1}{2} \frac{1}{2}\}:(x, y, z) \rightarrow (x + \frac{1}{2}, -y + \frac{1}{2}, -z + \frac{1}{2})$
$\{-1 0\}:(x, y, z) \rightarrow (-x, -y, -z)$	$\mathcal{T}\{m_{010} 0 \frac{1}{2} 0\}:(x, y, z) \rightarrow (x, -y + \frac{1}{2}, z)$
$\{m_{001} \frac{1}{2} 0 \frac{1}{2}\}:(x, y, z) \rightarrow (x + \frac{1}{2}, y, -z + \frac{1}{2})$	$\mathcal{T}\{m_{100} \frac{1}{2} \frac{1}{2} \frac{1}{2}\}:(x, y, z) \rightarrow (-x + \frac{1}{2}, y + \frac{1}{2}, z + \frac{1}{2})$

TABLE VII. Different symmetry operations of the magnetic space group for C-type AFM without SOI: $Pn'ma'$.

G_U (Unitary)	G_{AU} (Antiunitary) = $\mathcal{T}(G - G_U)$
$\{1 0\}:(x, y, z) \rightarrow (x, y, z)$	$\mathcal{T}\{2_{001} \frac{1}{2} 0 \frac{1}{2}\}:(x, y, z) \rightarrow (-x + \frac{1}{2}, -y, z + \frac{1}{2})$
$\{2_{010} 0 \frac{1}{2} 0\}:(x, y, z) \rightarrow (-x, y + \frac{1}{2}, -z)$	$\mathcal{T}\{2_{100} \frac{1}{2} \frac{1}{2} \frac{1}{2}\}:(x, y, z) \rightarrow (x + \frac{1}{2}, -y + \frac{1}{2}, -z + \frac{1}{2})$
$\{-1 0\}:(x, y, z) \rightarrow (-x, -y, -z)$	$\mathcal{T}\{m_{001} \frac{1}{2} 0 \frac{1}{2}\}:(x, y, z) \rightarrow (x + \frac{1}{2}, y, -z + \frac{1}{2})$
$\{m_{010} 0 \frac{1}{2} 0\}:(x, y, z) \rightarrow (x, -y + \frac{1}{2}, z)$	$\mathcal{T}\{m_{100} \frac{1}{2} \frac{1}{2} \frac{1}{2}\}:(x, y, z) \rightarrow (-x + \frac{1}{2}, y + \frac{1}{2}, z + \frac{1}{2})$

TABLE VIII. The antiunitary operations belonging to the magnetic space group that keep the \vec{k} -vector invariant in different planes of the Brillouin zone are listed here.

MSG	BZ plane	Antiunitary symmetry operation
$Pnm'a'$	$k_x = 0$	None, spin-splitting
	$k_y = 0$	$\mathcal{T}\{2_{010} 0 \frac{1}{2} 0\}:(u, 0, w) \rightarrow (u, 0, w)$
	$k_z = 0$	$\mathcal{T}\{2_{001} \frac{1}{2} 0 \frac{1}{2}\}:(u, v, 0) \rightarrow (u, v, 0)$
$Pn'm'a$	$k_x = 0$	$\mathcal{T}\{2_{100} \frac{1}{2} \frac{1}{2} \frac{1}{2}\}:(0, v, w) \rightarrow (0, v, w)$
	$k_y = 0$	$\mathcal{T}\{2_{010} 0 \frac{1}{2} 0\}:(u, 0, w) \rightarrow (u, 0, w)$
	$k_z = 0$	None, spin-splitting
$Pn'ma'$	$k_x = 0$	$\mathcal{T}\{2_{100} \frac{1}{2} \frac{1}{2} \frac{1}{2}\}:(0, v, w) \rightarrow (0, v, w)$
	$k_y = 0$	None, spin-splitting
	$k_z = 0$	$\mathcal{T}\{2_{001} \frac{1}{2} 0 \frac{1}{2}\}:(u, v, 0) \rightarrow (u, v, 0)$

CMO). The \vec{k} -vectors at the nodes at $k_y = 0$ and $k_z = 0$ may be represented by generic coordinates $(0, 0, w)$ and $(0, v, 0)$, respectively, which belong to the two spin degenerate k_x - k_z and k_x - k_y planes, respectively. Thus, our previous argument explains how the spin degeneracy is protected at these nodes.

C. Prediction of spin-splitting for other MSGs

Here we explore the possibility of spin-splitting in two other possible MSGs within the $Pnma$ space group without considering SOI. We begin by elaborating on the other two magnetic structures, A and C-type, for the unit cell. For A-type and C-type antiferromagnetic ordering, illustrated in Fig. 1(d) and Fig. 1(e), respectively, the MSG without SOI becomes $Pn'm'a$ and $Pn'ma'$, respectively [23, 37, 41]. The explicit symmetry operations are listed in Table VI and Table VII, respectively. The high-symmetry points in the BZ exhibit all the unitary and antiunitary symmetry operations of the MSGs $Pn'm'a$ and $Pn'ma'$, protecting the spin degeneracy at all high-symmetry points. Similar to our previous symmetry analysis, here we find that a generic \vec{k} -vector in

the k_x - k_y plane remains invariant under the symmetry operations $\{1|0\}$ and $\{m_{001}|\frac{1}{2} 0 \frac{1}{2}\}$ belonging to the MSG $Pn'm'a$, and the symmetry operations $\{1|0\}$ and $\mathcal{T}\{2_{001}|\frac{1}{2} 0 \frac{1}{2}\}$ belonging to the MSG $Pn'ma'$. Thus, although the spin degeneracy should be protected in the k_x - k_y plane for a C-type antiferromagnet, a spin splitting should be observed in the same plane for an A-type antiferromagnet. Table VIII tabulates the possible antiunitary symmetry operations for different planes in the BZ for the magnetic space groups $Pnm'a'$, $Pn'm'a$, and $Pn'ma'$, revealing the planes where no antiunitary symmetry operation protects band degeneracy of the opposite spin sublattices, leading to spin-splitting. As summarized in Table VIII, the BZ planes $k_x = 0$, $k_y = 0$, and $k_z = 0$ host spin-splitting for magnetic space groups $Pnm'a'$, $Pn'm'a$, and $Pn'ma'$, corresponding to G-type, A-type, and C-type antiferromagnetic configurations, respectively, where the first one has been verified from our DFT calculations.

D. Effective two-band model Hamiltonian at Γ point without SOI

After identifying the symmetry operations that enforce the spin degeneracy in some parts of the BZ, below we deduce a symmetry-adapted Hamiltonian that allows spin splitting in the remaining part of the BZ.

1. Effective two-band model Hamiltonian for the MSG $Pnm'a'$

First we construct the model Hamiltonian of the G-type antiferromagnet belonging to the $Pnm'a'$ MSG. Our approach involves defining two highly localized spin basis states at the magnetic sites according to the G-type antiferromagnetic ordering for both compounds. Subsequently, the effective two-band model Hamiltonian at a specific \vec{k} is derived by incorporating the symmetry con-

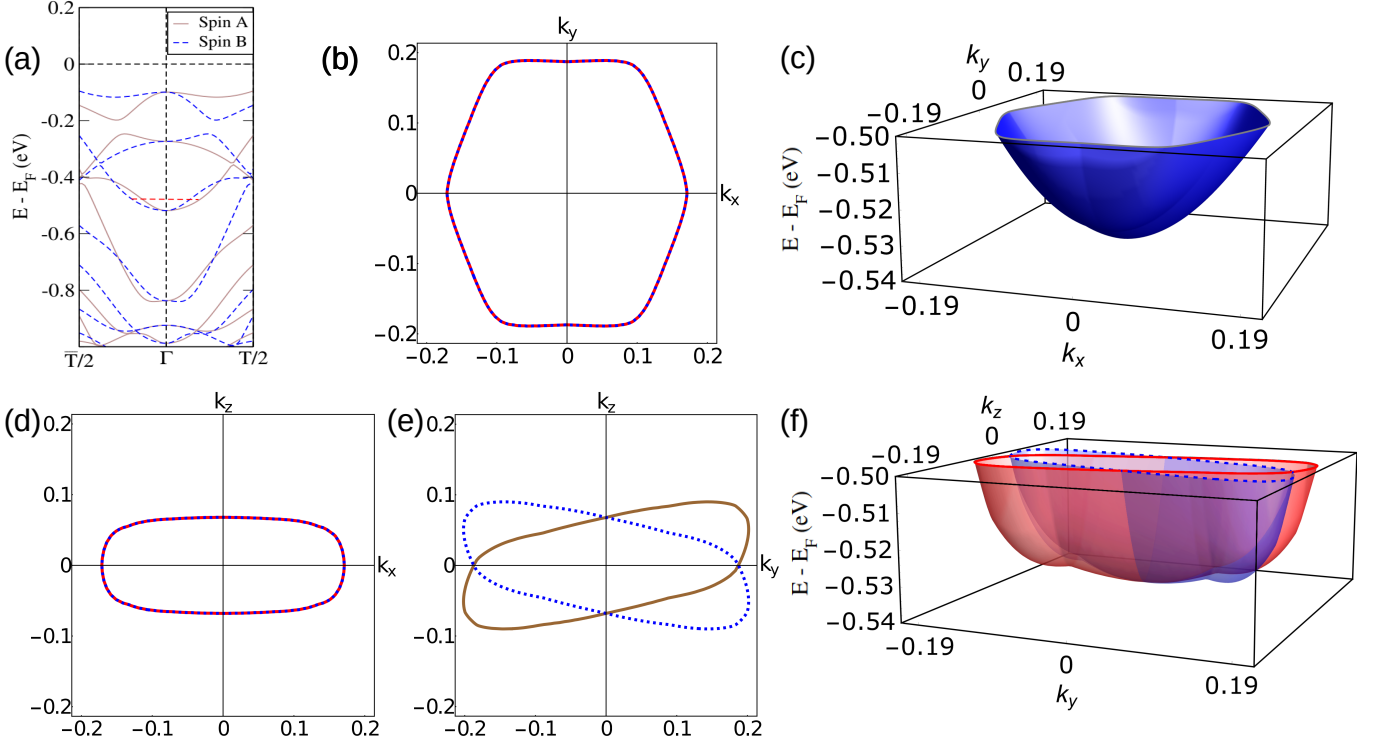


FIG. 5. The electronic structure and spin degeneracy of BiFeO₃ is critically analyzed in this figure. Panel (a) shows the spin-polarized bands along $\bar{T}/2 \rightarrow \Gamma \rightarrow \bar{T}/2$ direction. We choose a pair of spin-split bands in the valence band within an energy window $[-0.6, -0.4]$ eV intersecting a red dashed line at $E - E_F = -0.5$ eV. The isoenergetic contour in the $k_z = 0$ plane for $E - E_F = -0.5$ eV and the 3D band dispersion as a function of (k_x, k_y) are depicted in (b) and (c), respectively. Panel (d) and (e) depict the isoenergetic contours of the same pair of bands in the $k_y = 0$ and $k_x = 0$ planes, respectively, for $E - E_F = -0.5$ eV, while the 3D dispersion as a function of (k_y, k_z) with $k_x = 0$ is shown in (f).

TABLE IX. The transformation properties and the irreducible tensor up to the second order are listed according to the generator of the group of wave vector at Γ point for $Pnm'a'$ MSG.

Symmetrized matrix	Irreducible tensor	$\{2_{100} \frac{1}{2} \frac{1}{2} \frac{1}{2}\}$	$\{-1 0\}$	$\mathcal{T}\{2_{001} \frac{1}{2} 0 \frac{1}{2}\}$
σ_0	k_x^2, k_y^2, k_z^2	1	1	1
-	$k_x k_y$	-1	1	1
-	$k_x k_z$	-1	1	-1
σ_z	$k_y k_z$	1	1	-1

TABLE X. The transformation properties and the irreducible tensor up to the second order are listed according to the generator of the group of wave vector at Γ point for $Pn'm'a$ MSG.

Symmetrized matrix	Irreducible tensor	$\{2_{001} \frac{1}{2} 0 \frac{1}{2}\}$	$\{-1 0\}$	$\mathcal{T}\{2_{100} \frac{1}{2} \frac{1}{2} \frac{1}{2}\}$
σ_0	k_x^2, k_y^2, k_z^2	1	1	1
σ_z	$k_x k_y$	1	1	-1
-	$k_x k_z$	-1	1	-1
-	$k_y k_z$	-1	1	1

TABLE XI. The transformation properties and the irreducible tensor up to the second order are listed according to the generator of the group of wave vector at Γ point for $Pn'ma'$ MSG.

Symmetrized matrix	Irreducible tensor	$\{2_{010} 0 \frac{1}{2} 0\}$	$\{-1 0\}$	$\mathcal{T}\{2_{100} \frac{1}{2} \frac{1}{2} \frac{1}{2}\}$
σ_0	k_x^2, k_y^2, k_z^2	1	1	1
-	$k_x k_y$	-1	1	-1
σ_z	$k_x k_z$	1	1	-1
-	$k_y k_z$	-1	1	1

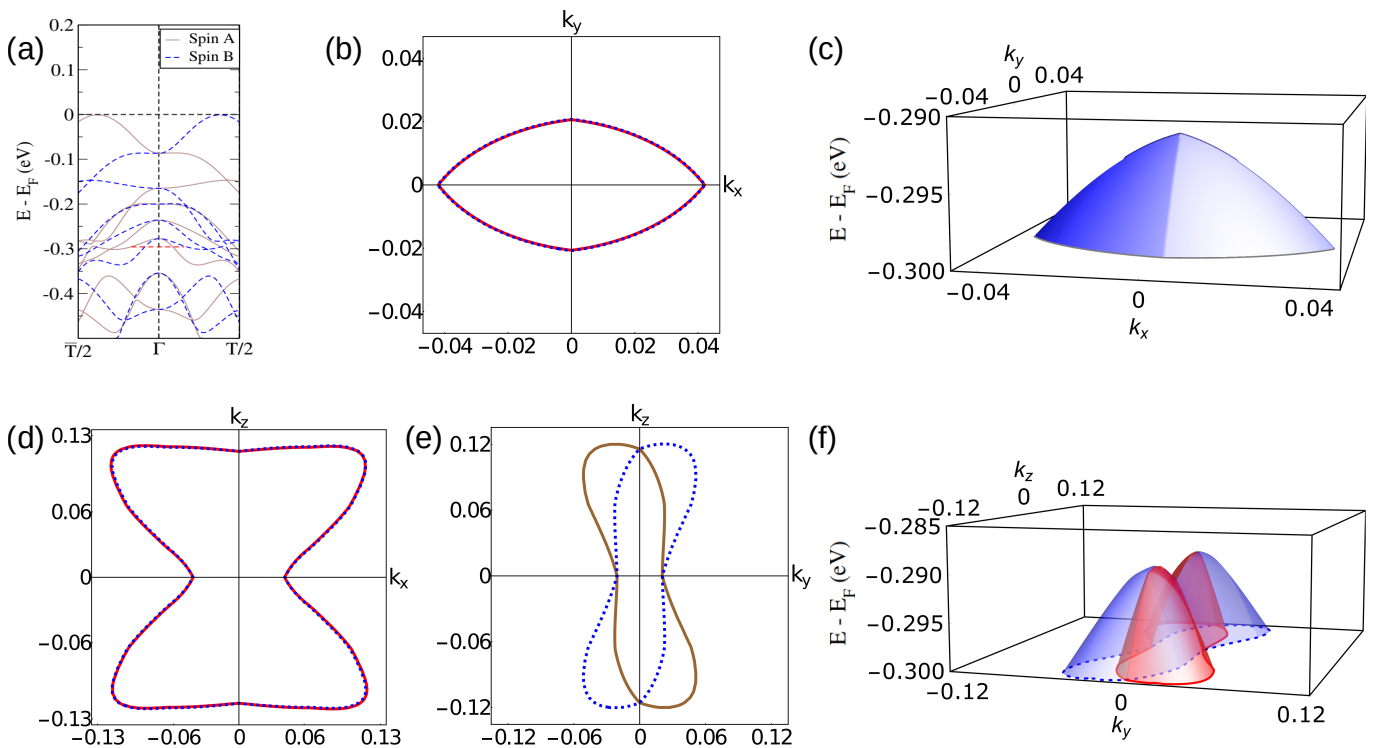


FIG. 6. The electronic structure and spin degeneracy of CaMnO_3 is critically analyzed in this figure. Panel (a) shows the spin-polarized bands along $\bar{T}/2 \rightarrow \Gamma \rightarrow \bar{T}/2$ direction. We choose a pair of spin-split bands in the valence band intersecting a red dashed line at $E - E_F = -0.3$ eV. The isoenergetic contour in the $k_z = 0$ plane for $E - E_F = -0.3$ eV and the 3D band dispersion as a function of (k_x, k_y) are depicted in (b) and (c), respectively. Panel (d) and (e) depict the isoenergetic contours of the same pair of bands in the $k_y = 0$ and $k_x = 0$ planes, respectively, for $E - E_F = -0.3$ eV, while the 3D dispersion as a function of (k_y, k_z) with $k_x = 0$ is shown in (f).

straints imposed by the group of wave vector on the basis. In this context, the group of wave vector at Γ point satisfies all the symmetry operations of the magnetic space group ($Pnm'a'$) without spin-orbit interaction (SOI), as listed in Table V. By selectively focusing on those symmetry operations associated with the generators of the group, we present the representations and transformation properties of both the Pauli vector $\vec{\sigma}$ and the wave vector \vec{k} .

The generator of the MSG $Pnm'a'$ contains two unitary operations $\{2_{100}|\frac{1}{2} \frac{1}{2} \frac{1}{2}\}, \{-1|0\}$ and one antiunitary operation $\mathcal{T}\{2_{001}|\frac{1}{2} 0 \frac{1}{2}\}$. The transformation properties of the Pauli matrix and the irreducible tensor operator \vec{k} upto the second order under these generators are listed in Table IX. Analyzing the Table IX, the only possible invariant term in the Hamiltonian is found to be $\sigma_z k_y k_z$, hinting a quadratic in \vec{k} nature of the nonrelativistic spin-splitting in the k_y - k_z plane, consistent with the Ref. [9]. Hence, the Hamiltonian takes the form

$$H = H_0 + \alpha \sigma_z k_y k_z, \quad (4)$$

where H_0 represents the Hamiltonian without considering the spin-splitting that may be represented by a standard tight-binding Hamiltonian, and α is a constant coefficient. The eigenvalues of the Hamiltonian mentioned

in Eq. (4) are $\varepsilon_0(\vec{k}) \pm \alpha k_y k_z$, with $\varepsilon_0(\vec{k})$ representing the band dispersion without the spin-splitting, which qualitatively explain the obtained results shown in the Fig. 5(e),(f) and Fig. 6(e),(f) for both compounds.

2. Effective two-band model Hamiltonian for the MSGs $Pn'm'a'$ and $Pn'ma'$

We extend our Hamiltonian formulation to the high-symmetry Γ point for two predicted MSGs: $Pn'm'a'$ and $Pn'ma'$, corresponding to A and C-type AFM structures, respectively. Following an approach similar to the above, we define two localized spin basis states at the magnetic sites according to the A and C-type AFM ordering. Then, the effective two-band model Hamiltonian at the Γ -point can be constructed by considering the symmetry constraints imposed by the group of wave vector on the basis. The group of wave vector at Γ point maintain all the symmetries of the MSGs $Pn'm'a'$ and $Pn'ma'$. From all the symmetries of both groups $Pn'm'a'$ and $Pn'ma'$ listed in Table VI and Table VII, we consider only the generators of the group to determine the representation and transformation properties of the Pauli vector $\vec{\sigma}$ and the wave vector \vec{k} . The generators and the transforma-

tion properties of $\vec{\sigma}$ and \vec{k} are presented in the Table X and Table XI for the MSG $Pn'm'a$ and $Pn'ma'$. By analyzing these tables, we find that the only invariant terms that could exist in the Hamiltonian are $\sigma_z k_x k_y$ for MSG $Pn'm'a$ and $\sigma_z k_x k_z$ for MSG $Pn'ma'$.

IV. CONCLUSION

To conclude our work, we studied bulk orthorhombic BFO and CMO within the first-principle density functional theory to understand its electronic structure and antiferromagnetic spin-splitting. Beginning with a chosen exchange-correlation functional and proper Hubbard correction, our investigation unveiled an insulating state in both compounds characterized by a preferred antiferromagnetic order. We observe a notable spin-splitting phenomenon within the lowest energy antiferromagnetic configuration for both systems, particularly evident in the k_y - k_z plane while maintaining spin degeneracy in other planes. The spin-splitting behavior remained largely unaffected even upon introducing spin-orbit interaction. Our critical examination of the spin-splitting features without spin-orbit interaction via conventional band dispersion, 3D band, and isoenergetic contours obtained from our DFT calculations confirms these two compounds as altermagnets. We also present an analytical explanation of our DFT results by analyzing magnetic symmetry in detail and an insightful analytical

model Hamiltonian based on the magnetic space group analysis. Additionally, we explore two other magnetic space groups corresponding to A-type and C-type antiferromagnetic arrangements within the $Pnma$ space group that may host the spin-splitting in different Brillouin zone planes and their probable form of the Hamiltonian. Our studies help thoroughly understand of the electronic and magnetic structure of bulk orthorhombic BFO and CMO, shedding light on antiferromagnetic spin-splitting phenomena. We extend our analysis to include two additional magnetic space groups, further exploring the potential for spin-splitting phenomena, thus, significantly advancing our understanding of spin-splitting in antiferromagnets without spin-orbit interaction within the orthorhombic $Pnma$ space group.

ACKNOWLEDGMENTS

S.R. and S.S. acknowledge research fellowships from CSIR, India through grant number 09/1020(0157)/2019-EMR-I, and from UGC, India, through UGC-Ref. No.:1470, respectively. N.G. acknowledges research fund from SERB, India through grant number CRG/2021/005320. The use of high-performance computing facilities at IISER Bhopal and PARAM Seva within the framework of the National Supercomputing Mission, India is gratefully acknowledged.

-
- [1] B. Keimer and J. E. Moore, The physics of quantum materials, *Nat. Phys.* **13**, 1045 (2017).
 - [2] A. Manchon, H. C. Koo, J. Nitta, S. M. Frolov, and R. A. Duine, New perspectives for Rashba spin-orbit coupling, *Nat. Materials*. **14**, 1476 (2015).
 - [3] V. Baltz, A. Manchon, M. Tsoi, T. Moriyama, T. Ono, and Y. Tserkovnyak, Antiferromagnetic spintronics, *Rev. Mod. Phys.* **90**, 015005 (2018).
 - [4] S. Rooj, J. Chakraborty, and N. Ganguli, Hexagonal MnTe with Antiferromagnetic Spin Splitting and Hidden Rashba - Dresselhaus Interaction for Antiferromagnetic Spintronics, *Adv. Phys. Res.* **3**, 2300050 (2024).
 - [5] L. Šmejkal, R. González-Hernández, T. Jungwirth, and J. Sinova, Crystal time-reversal symmetry breaking and spontaneous hall effect in collinear antiferromagnets, *Science Advances* **6**, aaz8809 (2020).
 - [6] L. Šmejkal, J. Sinova, and T. Jungwirth, Beyond conventional ferromagnetism and antiferromagnetism: A phase with nonrelativistic spin and crystal rotation symmetry, *Phys. Rev. X* **12**, 031042 (2022).
 - [7] L. Šmejkal, J. Sinova, and T. Jungwirth, Emerging research landscape of altermagnetism, *Phys. Rev. X* **12**, 040501 (2022).
 - [8] L.-D. Yuan, Z. Wang, J.-W. Luo, and A. Zunger, Prediction of low- z collinear and noncollinear antiferromagnetic compounds having momentum-dependent spin splitting even without spin-orbit coupling, *Phys. Rev. Mater.* **5**, 014409 (2021).
 - [9] L.-D. Yuan, Z. Wang, J.-W. Luo, E. I. Rashba, and A. Zunger, Giant momentum-dependent spin splitting in centrosymmetric low- z antiferromagnets, *Phys. Rev. B* **102**, 014422 (2020).
 - [10] R. González-Hernández, L. Šmejkal, K. Výborný, Y. Yahagi, J. Sinova, T. c. v. Jungwirth, and J. Železný, Efficient electrical spin splitter based on nonrelativistic collinear antiferromagnetism, *Phys. Rev. Lett.* **126**, 127701 (2021).
 - [11] H. Bai, L. Han, X. Y. Feng, Y. J. Zhou, R. X. Su, Q. Wang, L. Y. Liao, W. X. Zhu, X. Z. Chen, F. Pan, X. L. Fan, and C. Song, Observation of spin splitting torque in a collinear antiferromagnet ruo₂, *Phys. Rev. Lett.* **128**, 197202 (2022).
 - [12] R. D. Gonzalez Betancourt, J. Zubáč, R. Gonzalez-Hernandez, K. Geishendorf, Z. Šobáň, G. Springholz, K. Olejník, L. Šmejkal, J. Sinova, T. Jungwirth, S. T. B. Goennenwein, A. Thomas, H. Reichlová, J. Železný, and D. Krieger, Spontaneous anomalous hall effect arising from an unconventional compensated magnetic phase in a semiconductor, *Phys. Rev. Lett.* **130**, 036702 (2023).
 - [13] Z. Feng, X. Zhou, L. Šmejkal, L. Wu, Z. Zhu, H. Guo, R. González-Hernández, X. Wang, H. Yan, X. Qin, Peixin and Zhang, H. Wu, H. Chen, Z. Meng, L. Liu, Z. Xia, J. Sinova, T. Jungwirth, and Z. Liu, An anomalous Hall effect in altermagnetic ruthenium dioxide, *Nature Electronics* **5**, 2520 (2022).

- [14] K. P. Kluczyk, K. Gas, M. J. Grzybowski, P. Skupiński, M. A. Borysiewicz, T. Fąs, J. Suffczyński, J. Z. Domagala, K. Graszka, A. Mycielski, M. Baj, K. H. Ahn, K. Výborný, M. Sawicki, and M. Gryglas-Borysiewicz, Coexistence of anomalous hall effect and weak net magnetization in collinear antiferromagnet mnte, (2023), [arXiv:2310.09134](https://arxiv.org/abs/2310.09134).
- [15] M. Leiviskä, J. Rial, A. Badura, R. L. Seeger, I. Kounta, S. Beckert, D. Kriegner, I. Joumard, E. Schmoranzarová, J. Sinova, O. Gomonay, A. Thomas, S. T. B. Goennenwein, H. Reichlová, L. Šmejkal, L. Michez, T. Jungwirth, and V. Baltz, Anisotropy of the anomalous hall effect in the altermagnet candidate mn_5si_3 films, (2024), [arXiv:2401.02275](https://arxiv.org/abs/2401.02275) [[cond-mat.mes-hall](https://arxiv.org/abs/2401.02275)].
- [16] Y.-Y. Jiang, Z.-A. Wang, K. Samanta, S.-H. Zhang, R.-C. Xiao, W. J. Lu, Y. P. Sun, E. Y. Tsybal, and D.-F. Shao, Prediction of giant tunneling magnetoresistance in $\text{RuO}_2/\text{TiO}_2/\text{RuO}_2$ (110) antiferromagnetic tunnel junctions, *Phys. Rev. B* **108**, 174439 (2023).
- [17] L. Šmejkal, A. Marmodoro, K.-H. Ahn, R. González-Hernández, I. Turek, S. Mankovsky, H. Ebert, S. W. D'Souza, O. c. v. Šípr, J. Sinova, and T. c. v. Jungwirth, Chiral magnons in altermagnetic ruo_2 , *Phys. Rev. Lett.* **131**, 256703 (2023).
- [18] X. Zhou, W. Feng, R.-W. Zhang, L. Šmejkal, J. Sinova, Y. Mokrousov, and Y. Yao, Crystal thermal transport in altermagnetic ruo_2 , *Phys. Rev. Lett.* **132**, 056701 (2024).
- [19] T. Osumi, S. Souma, T. Aoyama, K. Yamauchi, A. Honma, K. Nakayama, T. Takahashi, K. Ohgushi, and T. Sato, Observation of a giant band splitting in altermagnetic mnte, *Phys. Rev. B* **109**, 115102 (2024).
- [20] I. A. Kornev, S. Lisenkov, R. Haumont, B. Dkhil, and L. Bellaïche, Finite-temperature properties of multiferroic bifeo₃, *Phys. Rev. Lett.* **99**, 227602 (2007).
- [21] Q. Zhou and B. J. Kennedy, Thermal expansion and structure of orthorhombic camno_3 , *Journal of Physics and Chemistry of Solids* **67**, 1595 (2006).
- [22] K. Momma and F. Izumi, VESTA 3 for three-dimensional visualization of crystal, volumetric and morphology data, *J. Appl. Cryst.* **44**, 1272 (2011).
- [23] M. I. Aroyo, J. M. Perez-Mato, C. Capillas, E. Kroumova, S. Ivantchev, G. Madariaga, A. Kirov, and H. Wondratschek, Bilbao crystallographic server: I. databases and crystallographic computing programs, *Zeitschrift für Kristallographie - Crystalline Materials* **221**, 15 (2006).
- [24] Q. Zhou and B. J. Kennedy, Thermal expansion and structure of orthorhombic camno_3 , *Journal of Physics and Chemistry of Solids* **67**, 1595 (2006).
- [25] G. Kresse and J. Furthmüller, Efficient iterative schemes for ab initio total-energy calculations using a plane-wave basis set, *Physical Review B* **54**, 11169 (1996).
- [26] G. Kresse and D. Joubert, From ultrasoft pseudopotentials to the projector augmented-wave method, *Physical Review B* **59**, 1758 (1999).
- [27] P. E. Blöchl, Projector augmented-wave method, *Phys. Rev. B* **50**, 17953 (1994).
- [28] J. P. Perdew, K. Burke, and M. Ernzerhof, Generalized Gradient Approximation Made Simple, *Phys. Rev. Lett.* **77**, 3865 (1996).
- [29] S. L. Dudarev, G. A. Botton, S. Y. Savrasov, C. J. Humphreys, and A. P. Sutton, Electron-energy-loss spectra and the structural stability of nickel oxide: An LSDA+U study, *Phys. Rev. B* **57**, 1505 (1998).
- [30] I.-T. Bae, A. Kovács, H. J. Zhao, J. Íñiguez, S. Yasui, T. Ichinose, and H. Naganuma, Elucidation of crystal and electronic structures within highly strained bifeo₃ by transmission electron microscopy and first-principles simulation, *Scientific Reports* **7**, 46498 (2017).
- [31] U. Aschauer, R. Pfenninger, S. M. Selbach, T. Grande, and N. A. Spaldin, Strain-controlled oxygen vacancy formation and ordering in camno_3 , *Phys. Rev. B* **88**, 054111 (2013).
- [32] P. E. Blöchl, O. Jepsen, and O. K. Andersen, Improved tetrahedron method for brillouin-zone integrations, *Phys. Rev. B* **49**, 16223 (1994).
- [33] R. Bharamagoudar, J. Angadi V, V. Pattar, A. S. Patil, S. Patil, R. S, S. Kulkarni, M. V. Malakannavar, and S. Matteppanavar, Low temperature magnetic properties of gd doped camno_3 , *Chemical Data Collections* **39**, 100846 (2022).
- [34] D. C. Arnold, K. S. Knight, F. D. Morrison, and P. Lightfoot, Ferroelectric-paraelectric transition in bifeo₃: Crystal structure of the orthorhombic β phase, *Phys. Rev. Lett.* **102**, 027602 (2009).
- [35] M. Mužević, I. Lukačević, I. Kovač, D. Gracin, A. Žužić, J. Macan, and M. V. Pajtler, Potential of amno_3 (a=ca, sr, ba, la) as active layer in inorganic perovskite solar cells, *ChemPhysChem* **24**, e202200837 (2023).
- [36] M. Molinari, D. A. Tompsett, S. C. Parker, F. Azough, and R. Freer, Structural, electronic and thermoelectric behaviour of camno_3 and $\text{camno}_{3-\delta}$, *J. Mater. Chem. A* **2**, 14109 (2014).
- [37] M. I. Aroyo, A. Kirov, C. Capillas, J. M. Perez-Mato, and H. Wondratschek, Bilbao Crystallographic Server. II. Representations of crystallographic point groups and space groups, *Acta Crystallographica Section A* **62**, 115 (2006).
- [38] M. S. Dresselhaus, G. Dresselhaus, and A. Jorio, *Group Theory: Application to the Physics of Condensed Matter* (Springer Berlin Heidelberg, Berlin, Heidelberg, 2008).
- [39] J. Perez-Mato, S. Gallego, E. Tasci, L. Elcoro, G. de la Flor, and M. Aroyo, Symmetry-based computational tools for magnetic crystallography, *Annual Review of Materials Research* **45**, 217 (2015).
- [40] C. J. Bradley and A. P. Cracknell, *The Mathematical Theory of Symmetry in Solids: Representation Theory for Point Groups and Space Groups* (Oxford University Press Inc., 2009).
- [41] J. Perez-Mato, S. Gallego, E. Tasci, L. Elcoro, G. de la Flor, and M. Aroyo, Symmetry-based computational tools for magnetic crystallography, *Annual Review of Materials Research* **45**, 217 (2015).